19th Australasian Fluid Mechanics Conference
Melbourne, Australia
8-11 December 2014

Direct Numerical Simulation of the Incompressible Temporally Developing Turbulent Boundary Layer

M. Kozul and D. Chung

Department of Mechanical Engineering
The University of Melbourne, Parkville VIC 3010, Australia

Abstract

We perform a direct numerical simulation investigation of the incompressible temporally developing turbulent boundary layer. The flow is the turbulent counterpart to the laminar Rayleigh problem or Stokes' first problem, in which a fluid at rest is set into motion by a wall moving at constant velocity. The physics contained in the idealised, short-domain, temporally developing boundary layer may prove useful in the study of wall turbulence at a manageable computational cost. This is in contrast to the considerable cost associated with long domains required for simulating the spatially developing boundary layer from trip to fully developed wall turbulence. Comparisons of the skin-friction coefficient, mean profile, turbulence intensity and Reynolds shear stress show that the temporally developing boundary layer and the spatially developing boundary layer are quite similar once initial conditions can be neglected. An initial profile that models the effect of a wall-mounted trip wire shows that the trip Reynolds number of 500 based on the trip-wire diameter is optimal for triggering transition while, at the same time, only mildly perturbing the flow so it tracks a self-similar development from the smallest Re_θ.

Introduction

Past studies [10, 11, 9] use long computational domains in order to simulate the spatially developing turbulent boundary layer. Such simulations are costly. For example, $8192 \times 513 \times 768 \approx 3.2 \times 10^9$ spectral modes are required in the simulations of [10]. In contrast to the spatially developing boundary layer, we propose here to study the temporally developing boundary layer. There are many past studies of both spatially developing [e.g. 13] and temporally developing [e.g. 8] free-shear flows. However, we are unaware of past studies of temporally developing incompressible turbulent boundary layers, although there are some studies of temporally developing compressible turbulent boundary layers [e.g. 5].

An important difference between the spatially developing and the temporally developing boundary layers can be found by comparing their respective momentum-integral equations. Consider the Navier–Stokes equations governing incompressible flow,

$$\frac{\partial u_i}{\partial t} + u_j \frac{\partial u_i}{\partial x_j} = -\frac{1}{\rho}\frac{\partial p}{\partial x_i} + \nu \frac{\partial^2 u_i}{\partial x_j^2}, \quad \frac{\partial u_j}{\partial x_j} = 0, \tag{1}$$

which represent the momentum and continuity equations, respectively. We will take x_1, x_2 and x_3 (or x, y and z) to mean the streamwise, spanwise and wall-normal directions. We choose the frame of reference in which the wall ($z = 0$) is moving at constant velocity ($u = U_w$) whilst the the far field ($z \to \infty$) remains at rest ($u \to 0$), well-known as the Rayleigh or Stokes' first problem (figure 1 *b*). The appropriate Reynolds decomposition for the temporally developing turbulent boundary layer is given by $u_i = \overline{u}(z,t)\delta_{i1} + u_i'(x,y,z,t)$, where $\overline{(\cdot)}$ indicates averaging in the homogeneous xy-plane. Substituting the decomposition in (1) and averaging in the homogeneous plane, we obtain

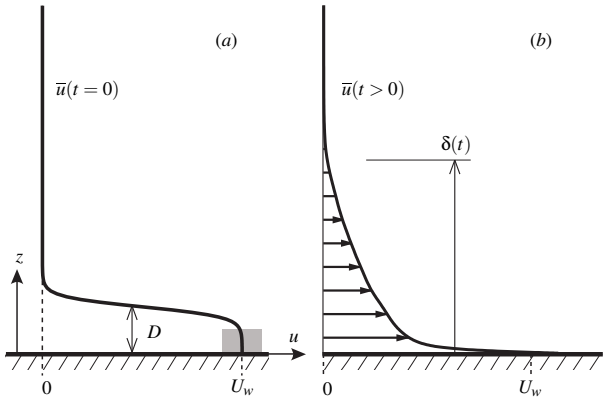

Figure 1. Illustration showing the streamwise velocity profile at (*a*) $t = 0$ and (*b*) $t > 0$. D is the 'trip-wire' diameter. The grey shaded area represents the magnitude of the white noise that is added to trigger transition.

$$\frac{\partial \overline{u}}{\partial t} = \nu \frac{\partial^2 \overline{u}}{\partial z^2} - \frac{\partial (\overline{w'u'})}{\partial z}. \tag{2}$$

In contrast, recall that a similar analysis for the spatially developing boundary layer yields $\overline{u}\partial\overline{u}/\partial x + \overline{v}\partial\overline{u}/\partial y$ on the left-hand side. Integrating (2) from the wall to the quiescent far field and imposing the appropriate boundary conditions for the viscous and Reynolds stresses, we obtain

$$\frac{\mathrm{d}\delta^*}{\mathrm{d}X} = \frac{C_f}{2} \equiv \frac{1}{2}\frac{\tau_0}{\frac{1}{2}\rho U_w^2} \equiv \frac{u_\tau^2}{U_w^2}, \tag{3}$$

where $\delta^* \equiv \int_0^\infty (\overline{u}/U_w)\, dz$, the displacement thickness; $X = U_w t$, the temporal counterpart to x in the spatially developing boundary layer; $\tau_0 \equiv -\mu\partial\overline{u}/\partial z|_0 > 0$, the wall shear stress; and u_τ is the friction velocity. For comparison, recall that the analogous expression for the spatially developing boundary layer is given by $\mathrm{d}\theta/\mathrm{d}x = C_f/2$, where θ is the momentum thickness. The preceding analysis suggests that δ^* plays an important role in the temporally developing boundary layer.

Resistance Laws

We now develop resistance laws that will be used for setting up the simulations. The analysis assumes Coles' law of the wall/wake for the turbulent boundary layer [2]:

$$\frac{U_w - \overline{u}}{u_\tau} = \frac{1}{\kappa}\log\left(\frac{z u_\tau}{\nu}\right) + A + \frac{\Pi}{\kappa} w\left(\frac{z}{\delta}\right) \tag{4}$$

where δ is the 99% boundary layer thickness; $w(z/\delta)$ is Coles' wake function, where $w(1) = 2$ by convention; Π measures the wake strength; and κ and A are the log-law constants. From the

Re_D	$Re_{\tau,f}$	$Re_{\delta,f}$	$L_xU_w/\nu \times L_yU_w/\nu \times L_zU_w/\nu$	$N_x \times N_y \times N_z$	Δx^+	Δy^+	Δz_1^+	Δz_t^+
250	72	2520	$90\,500 \times 45\,200 \times 43\,200$	$512 \times 512 \times 384$	8.81	4.41	0.252	8.81
500	788	18720	$90\,500 \times 45\,200 \times 43\,200$	$512 \times 512 \times 384$	9.88	4.94	0.283	9.88
1000	769	18000	$90\,500 \times 45\,200 \times 43\,200$	$512 \times 512 \times 384$	9.79	4.89	0.280	9.79
1500	792	18720	$90\,500 \times 45\,200 \times 43\,200$	$512 \times 512 \times 384$	8.79	4.40	0.252	8.79
2160	839	20160	$90\,500 \times 45\,200 \times 43\,200$	$512 \times 512 \times 384$	7.73	3.86	0.221	7.73

Table 1. Simulation parameters for the present temporally developing boundary layer simulations. Domain dimensions are given in terms of ν/U_w, which can be arbitrarily chosen. The grid spacings in wall units are the coarsest observed over the length of the simulation for each trip Reynolds number, Re_D. The wall-normal grid spacings, Δz_t and Δz_1, correspond, respectively, to those at the top and the bottom of the domain. The grid is set up such that $\Delta x \approx \Delta z_t$.

definition of the displacement thickness and (4), we arrive at:

$$\frac{\delta^*}{\delta} = C_1 \frac{u_\tau}{U_w} = \frac{C_1}{S}, \tag{5}$$

where $S \equiv U_w/u_\tau$ and C_1 is a constant. If we further assume that the wake function takes the form $w(z/\delta) = 1 - \cos(z/\delta)$, we can calculate $C_1 = (1+\Pi)/\kappa$. We seek an expression for $S = S(Re_X)$. To this end, we first rearrange (4) at $z = \delta$ to obtain

$$Re_\tau \equiv u_\tau \delta/\nu = \exp(\kappa[S - \phi(1)]) \tag{6}$$

or

$$Re_\delta \equiv U_w \delta/\nu = S\exp(\kappa[S - \phi(1)]), \tag{7}$$

where the shorthand, $\phi(1) = A + (\Pi/\kappa)w(1) = A + 2\Pi/\kappa$, is used. Rewriting the left-hand side of (7) as $(\delta/\delta^*)Re_{\delta^*}$, using (5), then substituting in (3) and invoking the change of variables that replaces $Re_{\delta^*}(Re_X)$ with $Re_{\delta^*}(S(Re_X))$, we arrive at the following expression:

$$\frac{1}{S^2} = \frac{d}{dS}\left[C_1 \exp(\kappa[S - \phi(1)])\right] \frac{dS}{dRe_X}, \tag{8}$$

Carrying out the differentiation with respect to S as written and then integrating by parts gives

$$Re_X = C_1 e^{\kappa[S-\phi(1)]}\left[S^2 - \frac{2S}{\kappa} + \frac{2}{\kappa^2}\right] - \frac{2}{\kappa^2} C_1 e^{-\kappa\phi(1)}, \tag{9}$$

where the initial condition, $S(Re_X = 0) = 0$, is assumed.

The constants κ, A and C_1 are determined from preliminary simulations and verified with the simulations presented in this paper. The log region of the mean velocity profiles well after transition gives κ. The time history of $S\delta^*/\delta$ in (5) reveals that the value of C_1 stabilises and approaches a constant well after transition. The definition of C_1 (assuming a cosine form for the wake) then allows us to deduce $\Pi = \kappa C_1 - 1$. This value of Π found from the definition of C_1 is also verified graphically from the outer-scaled velocity defect. Scaling with inner coordinates yields the intercept A. We can then calculate $\phi(1) = A + 2\Pi/\kappa$. The relevant constants for the present flow are $\kappa \approx 0.40, A \approx 5.0$ and $C_1 \approx 3.6$, from which we have $\Pi \approx 0.44$ and $\phi(1) \approx 7.2$. These values agrees well with the compilation of [7].

Simulation setup

We first determine the domain size and the grid spacing in terms of the reference length scale, ν/U_w. The quantities, ν and U_w, can be arbitrarily chosen. The domain size, (L_x, L_y, L_z), is determined by the largest boundary layer thickness, δ_f, which occurs at the end of the simulation (the subscript f refers to final), while the grid spacing, $(\Delta x, \Delta y, \Delta z)$, is determined by the smallest wall unit, $\nu/u_{\tau,p}$, which occurs earlier in the simulation when the skin friction reaches its maximum (the subscript p refers to peak). In this study, we seek to obtain a boundary layer at the end of the simulation that is comparable to the $Re_\tau \approx 590$ channel flow of [6]. Thus, setting $Re_{\tau,f} \approx 590$ in (6), we obtain $S_f \approx 23.2$, which can then be substituted in (7) to obtain $Re_{\delta,f} \approx 13\,700$, say $Re_{\delta,f} \approx 14\,400$, that is, $\delta_f \approx 14\,400\nu/U_w$. Following [6], we set the wall-parallel domain size to $L_x = 2\pi\delta_f \approx 90\,500\nu/U_w$ and $L_y = \pi\delta_f \approx 45\,200\nu/U_w$, and following [10], we set the wall-normal domain size to $L_z = 3\,\delta_f \approx 43\,200\nu/U_w$. For the wall-parallel grid spacing, we follow [6] and enforce $\Delta x^+ < 9.7$ and $\Delta y^+ < 4.8$ at all times, which is satisfied by $\Delta x = 9.7\nu/u_{\tau,p}$ and $\Delta y = 4.8\nu/u_{\tau,p}$. Our preliminary simulations estimated that the maximum attainable peak skin-friction coefficient corresponds to $S_p \approx 18.7 \Leftrightarrow C_{f,p} \approx 5.7 \times 10^{-3}$, also corroborated by spatially developing boundary layer simulations [e.g. 9, 10]. We can now specify the number of grid points in the streamwise direction:

$$\begin{aligned} N_x &= \frac{L_x}{\Delta x} = \frac{2\pi\delta_f}{9.7\nu/u_{\tau,p}} = \frac{2\pi}{9.7} Re_{\tau,f}\,\frac{S_f}{S_p} \\ &= \frac{2\pi}{9.7}(590)\frac{(23.2)}{(18.7)} \approx 473, \end{aligned} \tag{10}$$

say $N_x \approx 512$ to be conservative. A similar calculation for the spanwise direction yields $N_y \approx 512$. The wall-normal grid spacing is uniform for the first three wall-adjacent cells, but obeys a half-cosine mapping from the fourth cell onwards, giving a finer grid at the wall, and a coarser grid away from the wall. The cosine can be expanded in a Taylor series to obtain

$$\Delta z_1 \approx L_z\left[\cos\left(\frac{3\pi}{2N_z}\right) - \cos\left(\frac{4\pi}{2N_z}\right)\right] \approx \frac{7}{8}\frac{\pi^2}{N_z^2}\,L_z. \tag{11}$$

We enforce $\Delta z_1^+ < 0.2$ at all times for the first wall-normal grid spacing, which is satisfied by $\Delta z_1 = 0.2\nu/u_{\tau,p}$. We can now set

$$\begin{aligned} N_z &\approx \sqrt{\frac{7\pi^2}{8}\frac{L_z}{\Delta z_1}} = \sqrt{\frac{7\pi^2}{8}\frac{3\,\delta_f}{0.2\nu/u_{\tau,p}}} = \sqrt{\frac{7\pi^2}{8}\frac{3}{0.2} Re_{\tau,f}\,\frac{S_f}{S_p}} \\ &= \sqrt{\frac{7\pi^2}{8}\frac{3}{0.2}(590)\frac{(23.2)}{(18.7)}} \approx 308, \end{aligned} \tag{12}$$

say $N_z \approx 384$ to be conservative. Table 1 summarises these grid parameters.

The boundary conditions are periodic in the x and y directions. No-slip and impermeable boundary conditions representing a moving wall, $u = v = U_w$ and $w = 0$, are imposed at the bottom boundary ($z = 0$). The top boundary ($z = L_z$) is a fixed wall, where no-slip and impermeable boundary conditions are also

applied, $u = v = w = 0$. The skin-friction coefficient at the top wall remains below 2.9×10^{-8} at all times for all the simulations presented in this paper.

For initial conditions, we set $u_{i,0} = \overline{u}_{i,0}(z) + u'_{i,0}(x,y,z)$, where

$$\overline{u}_0(z) = \frac{U_w}{2} + \frac{U_w}{2}\tanh\left[\frac{D}{2\theta_{sl}}\left(1 - \frac{z}{D}\right)\right], \qquad (13)$$

$\overline{v}_0 = \overline{w}_0 = 0$ [cf. 3]. Physically, such an initial velocity profile resembles the wake of a trip wire with diameter, D, and may be compared to physical trips placed at the beginning of a boundary layer wind tunnel. Hereafter, we will refer to $Re_D \equiv DU_w/\nu$ as the trip Reynolds number. The step-function-like shape of the tanh profile also means that the trip diameter can be identified with the initial boundary layer displacement thickness, that is, $D \approx \delta^*_0$. To trigger transition, white noise, $|u'_{i,0}| < 0.1U_w$, is added to all velocity components near the wall where $U_w - \overline{u}_0 < 10^{-4}U_w$ (see figure 1 *a*). The momentum thickness of the shear layer is set to $\theta_{sl} \approx 54\nu/U_w$. The Strouhal number of the primary Kelvin–Helmholtz instability is given by $S_{sl} \equiv f_{sl}\theta_{sl}/(U_w/2) \approx 0.033$ [e.g. 3], from which the associated instability length scale is $\lambda_{sl} = (U_w/2)/f_{sl}$. Therefore the number of Kelvin–Helmholtz rollers that form in our boundary layer can be estimated by $L_x/\lambda_{sl} \approx 0.033 L_x/\theta_{sl} \approx 55.3$. The small size of these rollers ensure that they will be quickly forgotten as time progresses, leading to a self-similar development from the smallest Re_θ.

Results

The present code has been validated in [1]. The grid spacings in wall units are monitored to ensure that the simulation is resolved at all times (table 1). The simulations are run a little longer, reaching $Re_\tau \approx 800$, compared to the planned $Re_\tau \approx 590$. This results in slightly smaller domain sizes ($L_x/\delta \approx 4.5$) than planned ($L_x/\delta \approx 6.0$).

Figure 2 shows the development of C_f versus Re_θ, Re_X and Re_{δ^*} with the five different values for Re_D. The turbulent branch of $C_f(Re_X)$ as predicted by (9) and other similar relations for $C_f(Re_\theta)$ and $C_f(Re_{\delta^*})$ are plotted on top of the data. We also plot the laminar branch of C_f derived from the well-known erfc profile. Figure 2 suggests that, provided the trip is large enough ($Re_D \gtrsim 500$) to trigger transition to turbulence, the temporal development of the turbulent boundary layer as measured by C_f eventually follows a self-similar evolution. When $Re_D \lesssim 250$, transition is not observed. These figures are similar to the critical $Re_{\delta^*} \approx 420$ for transition (for the Blasius profile) given by [4] (recall that $D \approx \delta^*_0$). Provided transition is initiated, the flow that is least perturbed (smallest Re_D) leads to a self-similar development from the smallest Re_θ. This can be observed in figure 2(*a*,*b*), where first the $Re_D \approx 1000$ curve, then the $Re_D \approx 1500$ curve, and finally the $Re_D \approx 2160$ curve, track the $Re_D \approx 500$ curve. Convincing collapse of C_f is best observed with Re_{δ^*}, in agreement with the analysis in the Introduction, although a fair collapse of C_f is also observed with Re_θ. We do not observe convincing collapse in figure 2(*c*) owing to the ill-defined virtual origin. Recall that the initial condition $S(Re_X = 0) = 0$ is used in the derivation leading to (9). However, we expect to see collapse if we allow for a simple shift in Re_X by $Re_{X,0}$. In any case, the virtual-origin effect becomes unimportant at large Re_X because $Re_X - Re_{X,0} \sim Re_X$. Data from the spatially developing boundary layer of [9] is plotted in figure 2 for for comparison. Even though the laminar branches of C_f are clearly different, the turbulent branches of C_f are a fair represention for both spatial and temporal simulations. This is consistent with the idea that parallel-flow approximation for the spatially developing boundary layer becomes better with increasing Re_x.

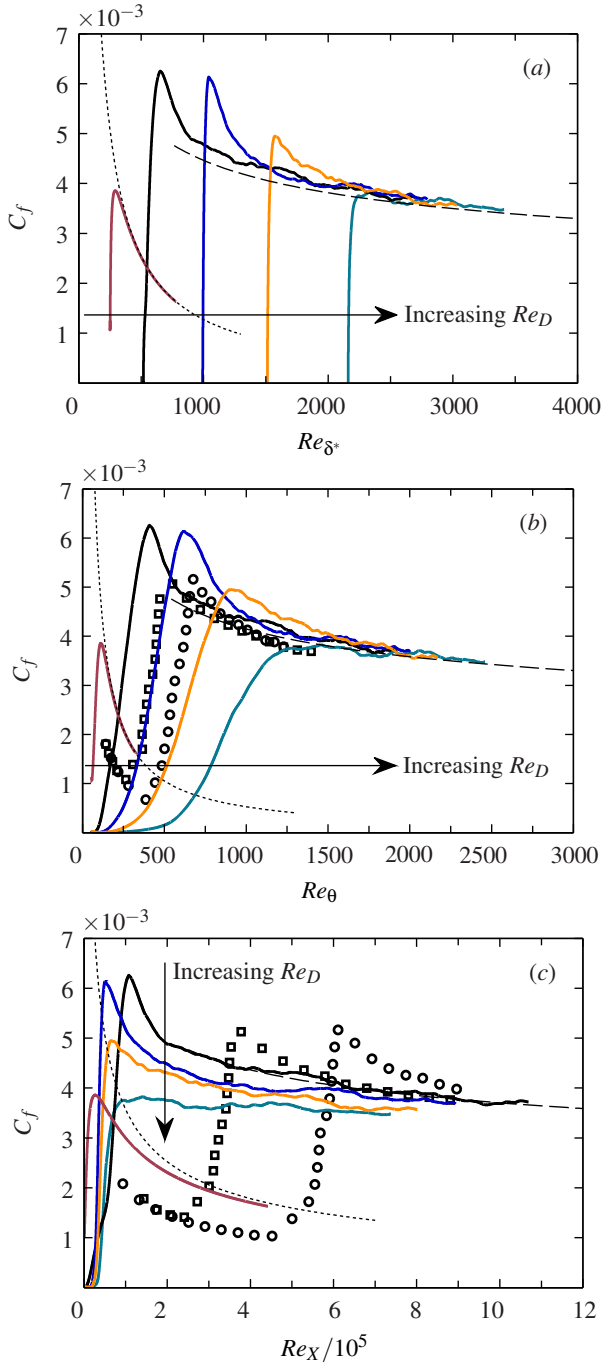

Figure 2. Variation of skin-friction coefficient versus (a) Re_{δ^*}, (b) Re_θ and (c) Re_X: ——, $Re_D = 250$; ——, 500; ——, 1000; ——, 1500 and ——, 2160; – – –, turbulent resistance law; - - - - -, laminar resistance law. Data from [9] is plotted for comparison: □, K-type transition; ○, H-type transition.

The mean and turbulence statistics at $Re_\theta \approx 1100$ and $Re_\theta \approx 2000$ for trips $Re_D = 500$ and above are shown in figure 3. Consistent with the story told by the C_f curves, it is clear that the least perturbed boundary layer at $Re_D \approx 500$ is the flow that assumes a self-similar development from the smallest Re_θ. At $Re_\theta \approx 1100$, the larger two trips ($Re_D \geq 1500$) have not yet tracked the other curves; later at the larger $Re_\theta \approx 2000$, the $Re_D \approx 1500$ flow appears to have relaxed to a self-similar development, although the $Re_D \approx 2160$ remains perturbed. We also observe an earlier convergence in the mean profile compared to the turbulent statistics, an effect clearly seen at $Re_\theta \approx 2000$ for $Re_D \approx 2160$, consistent with spatially developing boundary

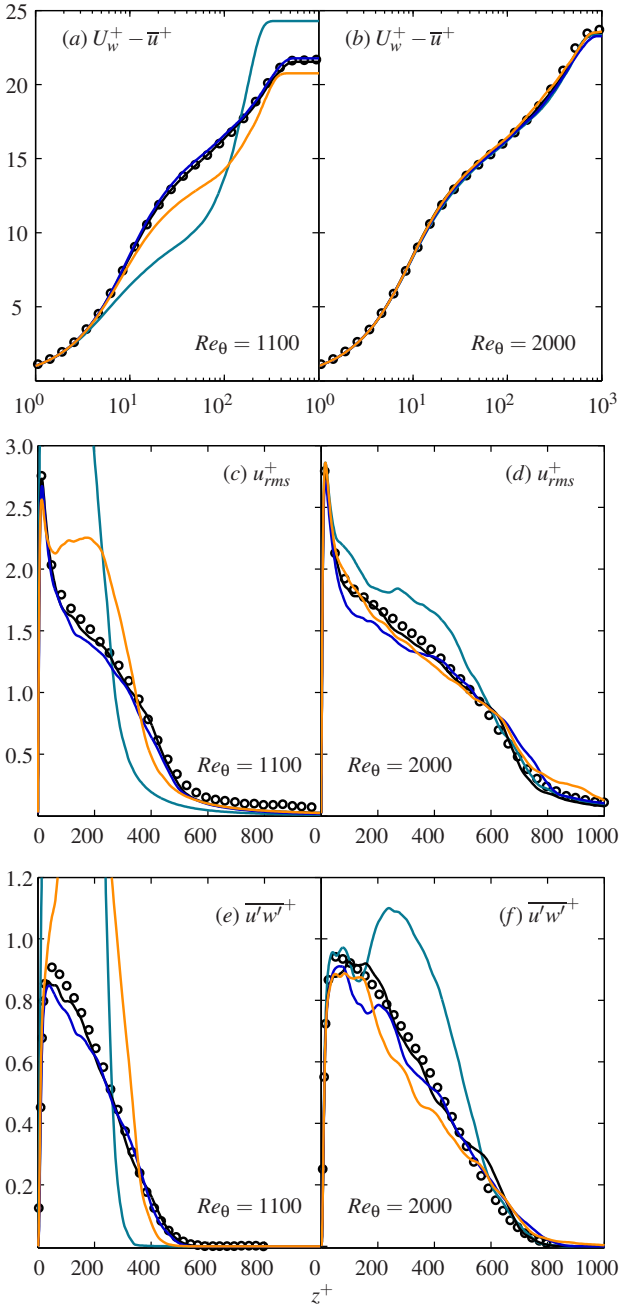

Figure 3. Mean and turbulent statistics at two different Re_θ: ——, $Re_D \approx 500$; ——, $Re_D \approx 1000$; ——, $Re_D \approx 1500$; ——, $Re_D \approx 2160$. In (c), the data from [12] is for $-\overline{u'w'}^+$; the sign is reversed here for the present temporal configuration.

layers [11]. For comparison, data from the spatially developing boundary layer of [12] is also shown. The agreement between the two flows suggests that the temporally developing boundary layer is a good model for studying the spatially developing boundary layer.

Conclusions

We have investigated the incompressible temporally developing turbulent boundary layer and compared it to its spatially developing counterpart. The present results suggest that the two flows are similar in many respects, including turbulent skin-friction development (figure 2) as well as mean and turbulent profiles (figure 3). As expected, the effect of initial conditions cannot be neglected. Presently, this effect is investigated using a tanh profile that models the wake of a wall-mounted trip. We observe that, for the large trip of $Re_D \approx 2160$, the boundary remains perturbed even at $Re_\theta \approx 2000$. For the small trip of $Re_D \approx 250$, the boundary layer remains laminar, but for $Re_D \approx 500$, the boundary layer transitions and quickly assumes a self-similar development at the smallest Re_θ. The results suggest the memory effect depends on an appropriate Reynolds number based on the tripping device and that this effect can never be neglected but can and should be managed in simulations and in laboratory experiments.

Acknowledgements

Part of this research was undertaken on the NCI National Facility in Canberra, Australia, which is supported by the Australian Commonwealth Government. M. Kozul gratefully acknowledges funding provided by the Australian Research Council.

References

[1] Chung, D., Monty, J. P. and Ooi, A., An idealised assessment of townsend's outer-layer similarity hypothesis for wall turbulence, *J. Fluid Mech.*, **742**, 2014, R3.

[2] Coles, D., The law of the wake in the turbulent boundary layer, *J. Fluid Mech.*, **1**, 1956, 191–226.

[3] da Silva, C. B. and Pereira, J. C. F., Invariants of the velocity-gradient, rate-of-strain, and rate-of-rotation tensors across the turbulent/nonturbulent interface in jets, *Phys. Fluids*, **20**, 2008, 055101.

[4] Landau, L. D. and Lifshitz, E. M., *Fluid Mechanics*, Pergamon Press, 1987, 2nd edition.

[5] Martin, M. P., Direct simulation of hypersonic turbulent boundary layers. Part 1. initialization and comparison with experiments, *J. Fluid Mech.*, **570**, 2007, 347–364.

[6] Moser, R. D., Kim, J. and Mansour, N. N., Direct numerical simulation of turbulent channel flow up to $Re_\tau = 590$, *Phys. Fluids*, **11**, 1999, 943–945.

[7] Nagib, H. M. and Chauhan, K. A., Variations of von Kármán coefficient in canonical flows, *Phys. Fluids*, **20**, 2008, 101518.

[8] Rogers, M. M. and Moser, R. D., Direct simulation of a self-similar turbulent mixing layer, *Phys. Fluids*, **6**, 1994, 903–923.

[9] Sayadi, T., Hamman, C. W. and Moin, P., Direct numerical simulation of complete h-type and k-type transitions with implications for the dynamics of turbulent boundary layers, *J. Fluid Mech.*, **724**, 2013, 480–509.

[10] Schlatter, P. and Örlü, R., Assessment of direct numerical simulation data of turbulent boundary layers, *J. Fluid Mech.*, **659**, 2010, 116–126.

[11] Schlatter, P. and Örlü, R., Turbulent boundary layers at moderate reynolds numbers: inflow length and tripping effects, *J. Fluid Mech.*, **710**, 2012, 5–34.

[12] Simens, M. P., Jiménez, J., Hoyas, S. and Mizuno, Y., A high-resolution code for turbulent boundary layers, *J. Comput. Phys.*, **228**, 2009, 4218–4231.

[13] Stanley, S. and Sarkar, S., Simulations of spatially developing two-dimensional shear layers and jets, *Theor. Comput. Fluid Dyn.*, **9**, 1997, 121–147.